

# Global Precipitation Nowcasting of Integrated Multi-satellite Retrievals for GPM: A U-Net Convolutional LSTM Architecture

Reyhaneh Rahimi <sup>a</sup>, Praveen Ravirathinam <sup>b</sup>, Ardeshir Ebtehaj <sup>a</sup>, Ali Behrangi <sup>c</sup>, Jackson Tan <sup>d</sup>,  
and Vipin Kumar <sup>b</sup>

<sup>a</sup> *Department of Civil Environmental and Geo-Engineering and the Saint Anthony Falls  
Laboratory, University of Minnesota*

<sup>b</sup> *Department of Computer Science and Engineering, University of Minnesota*

<sup>c</sup> *Department of Hydrology and Atmospheric Sciences, The University of Arizona*

<sup>d</sup> *Earth Sciences Division, NASA's Goddard Space Flight*

arXiv:2307.10843v2 [cs.LG] 2 Feb 2024

*Corresponding author: Ardeshir Ebtehaj, email@ebtehaj@umn.edu*

**ABSTRACT:** This paper presents a deep learning architecture for 30 min global precipitation nowcasts with a 4-hour lead time. The architecture follows a U-Net structure with convolutional long short-term memory (ConvLSTM) cells along with a unique recursive ConvLSTM-based skip connection technique to maintain the sharpness of precipitation fields and reduce information loss due to the pooling operation of the U-Net. The training uses data from the Integrated MultisatellitE Retrievals for GPM (IMERG) and a few key drivers of precipitation from the Global Forecast System (GFS). The impacts of different training loss functions, including the mean-squared error (regression) and the focal-loss (classification), on the quality of precipitation nowcasts are studied. The results indicate that the regression network performs well in capturing light precipitation ( $<1.6 \text{ mm hr}^{-1}$ ) while the classification network can outperform the regression counterpart for nowcasting of high-intensity precipitation ( $>8 \text{ mm hr}^{-1}$ ), in terms of the critical success index (CSI). It is uncovered that the inclusion of the forecast variables can improve precipitation nowcasting, especially at longer lead times in both networks. Taking IMERG as a relative reference, a multi-scale analysis, in terms of fractions skill score (FSS), shows that the nowcasting machine remains skillful for precipitation rate above  $1 \text{ mm hr}^{-1}$  at the resolution of 10 km compared to 50 km for GFS. For precipitation rates greater than  $4 \text{ mm hr}^{-1}$ , only the classification network remains FSS-skillful on scales greater than 50 km within a 2-hour lead time.

**SIGNIFICANCE STATEMENT:** This study presents a deep neural network architecture for global precipitation nowcasting with a 4-hour lead time, using sequences of past satellite precipitation data and simulations from a numerical weather prediction model. The results show that the nowcasting machine can improve short-term predictions of high-intensity precipitation on a global scale. The outcomes of the research will enable us to expand our understanding of how modern deep learning can improve the predictability of extreme weather and benefit flood early warning systems for saving lives and properties.

## 1. Introduction

Precipitation nowcasting, short-term forecasts with a lead time of fewer than 6 hours, is important for weather-dependent decision-making (Sun et al. 2014a; Shi et al. 2015; Otsuka et al. 2019), especially in relationship with early flood warning systems (Imhoff et al. 2022). Modern Numerical Weather Prediction (NWP) models, such as the NOAA’s Global Forecast System (GFS, NCEP 2021) provide short-term hourly predictions of near-surface global precipitation at 0.25° grid size (Toth and Kalnay 1997; Sun et al. 2014a). However, NWP’s precipitation nowcasting often faces significant uncertainties due to errors arising in initialization (Hwang et al. 2015), data assimilation (Barker et al. 2004), and sub-grid scale parameterization of convective processes (Zhang et al. 2021; Sun 2005).

Initialization and data assimilation of NWP’s often involve a spin-up period of 3–6 hours (Buehner and Jacques 2020; Lin and Pu 2020; Lin et al. 2005) within which the forecast accuracy is suboptimal (Kendon et al. 2021). Moreover, precipitation is not a fundamental state variable (e.g., velocity, temperature, and moisture) in NWP’s (Lin et al. 2015). Consequently, variational data assimilation frameworks rely on linear tangent models and their adjoint operators. Since precipitation processes have a flow-dependent non-linear relationship with the basic state variables, even with a carefully designed adjoint operator, the nowcasting uncertainties can remain large (Errico et al. 2007; Zhang et al. 2013). At the same time, the global precipitation forecasts are not currently convective permitting (Prein et al. 2015) and rely on sub-grid scale parameterizations (Hohenegger et al. 2009; Kendon et al. 2012). The parameterization uncertainties often lead to position errors in the prediction of the extent, intensity, and phase of precipitation events, especially for summertime

mesoscale convective systems (Ban et al. 2014; Prein et al. 2015; Lin et al. 2015) and short-lived snowstorms (Liu et al. 2011).

Experimental evidence has suggested that statistical post-processing and machine learning models can temporally extrapolate the observed precipitation fields by ground-based radars (Bowler et al. 2004; Ayzel et al. 2019) and spaceborne platforms (Otsuka et al. 2016; Kumar et al. 2020) with a higher degree of accuracy than NWP, over limited forecast lead times (Sønderby et al. 2020). Data-driven precipitation nowcasting can be grouped into two classes: (i) advective-based approaches (Ayzel et al. 2019) that often rely on classic regression and optimal filtering (Germann and Zawadzki 2002; Reyniers 2008) and (ii) modern machine learning (ML) and artificial intelligence (AI) frameworks (Ravuri et al. 2021; Shi et al. 2015).

The advective approaches (Bowler et al. 2004; Pulkkinen et al. 2019) attempt to track the near-surface wind velocity fields and precipitating cells (Austin and Bellon 1974) using optical-flow methods (Bowler et al. 2004, 2006). Utilizing this approach, different operational nowcasting models have been developed including the *Pysteps* (Pulkkinen et al. 2019) and the *rainymotion* (Ayzel et al. 2019). These models can only represent a shifted version of previous observations and thus fail to simulate the dynamic evolution of precipitation fields (Agrawal et al. 2019). However, for example, the results by Lin et al. (2005) showed that the probability of precipitation detection can be around 85 (50)% for the advection-based nowcasting, compared with 50 (60)% for the Weather Research and Forecasting (WRF, Powers et al. 2017) model for a 1(6)-hour lead time.

The second class largely relies on deep learning neural networks (DNN, LeCun et al. 2015), primarily tailored for solving computer vision problems in image classification (Rawat and Wang 2017), video frame prediction (Mnih et al. 2015; Yang et al. 2019), and semantic segmentation (McCormac et al. 2017). In summary, a sequence of observed precipitation fields serves as inputs/outputs of a DNN to train it as a nowcasting machine (Shi et al. 2015). Research suggests that these machines can provide more accurate predictions of convective heavy precipitation compared to the advective counterparts (Shi et al. 2015; Agrawal et al. 2019; Ravuri et al. 2021; Trebing et al. 2021; Ehsani et al. 2022), largely due to their ability to learn complex nonlinear processes. For example, Pulkkinen et al. (2019) highlighted that advection models can offer potentially valuable forecasting skills for precipitation rates of  $0.1 \text{ mm hr}^{-1}$  for a duration of up to 3 hours. However,

for more intense rates (i.e.,  $5 \text{ mm hr}^{-1}$ ), useful nowcasts are only attainable for a maximum lead time of 45 minutes.

The mainstream ML models often use the convolutional neural network (CNN, [Krizhevsky et al. 2012](#)) and the recurrent neural network (RNN, [Hochreiter and Schmidhuber 1997](#)). The most commonly used CNN nowcasting models are based on U-Net ([Ronneberger et al. 2015](#)) architecture and its variants ([Han et al. 2021](#); [Ayzel et al. 2020](#); [Trebing et al. 2021](#)), where spatiotemporal dynamics of precipitation are captured by convolution operations. Recurrent neural networks ([Hochreiter and Schmidhuber 1997](#)), originally developed for modeling texts can capture temporal memory of the underlying processes. A combination of CNN and RNN namely the convolutional long short-term memory (ConvLSTM) architectures ([Shi et al. 2015](#)) have been deployed to simultaneously learn spatiotemporal dynamics of precipitation fields for providing regional nowcasts with a lead time of 90 minutes using ground-based radar data. Building on ConvLSTM, multiple variants have emerged to process the spatiotemporal rainfall data such as TrajGRU ([Shi et al. 2017](#)) and PredRNN ([Wang et al. 2017](#)).

More recently, [Ravuri et al. \(2021\)](#) introduced a deep generative neural network for probabilistic nowcasting using ground-based radar data over the United Kingdom that outperformed an advective approach ([Pulkkinen et al. 2019](#)) for lead times beyond 30 minutes. Despite its success, the model exhibited large uncertainties in the nowcasting of extreme precipitation and cloud dissipation at long lead times. To address this limitation, [Zhang et al. \(2023\)](#) proposed NowcastNet that informs the deep-learning machine by the continuity equations and extends the protective skills of the approach by [Ravuri et al. \(2021\)](#) – especially for rates above  $16 \text{ mm hr}^{-1}$ . More recently, [Jin et al. \(2023\)](#) used an encoder-decoder architecture built around ConvLSTM layers to highlight the impacts of temperature, humidity, and wind velocity on precipitation nowcasts.

Most of the developed nowcasting models used ground-based regional precipitation radar observations ([Han et al. 2021](#); [Sun et al. 2014a](#); [Pan et al. 2021](#)). Recently a few studies have employed satellite data based on advective ([Kotsuki et al. 2019](#); [Otsuka et al. 2016](#)) and ML frameworks ([Kumar et al. 2020](#); [Ehsani et al. 2022](#)). Using a local ensemble transform Kalman filter, a prototype system was developed by [Otsuka et al. \(2016\)](#) and tested using the Japan Aerospace Exploration Agency's Global Satellite Mapping of Precipitation (GSMaP) ([Kubota et al. 2007](#)). More recently, the Integrated Multi-satellitE Retrievals for GPM (IMERG, [Huffman et al. 2020](#)) were used over the

eastern CONUS for training and testing both a convolutional deep neural network and a recurrent neural network for precipitation nowcasting with 90 minutes lead time (Ehsani et al. 2022).

In this paper, we present a Global prEciPitation Nowcasting using intEgrated multi-Satellite retrIevalS for GPM (GENESIS) that can effectively forecast short-term spatiotemporal dynamics of global precipitation. The GENESIS architecture replaces standard convolution layers in U-Net with ConvLSTM layers, to capture the space-time nature of the precipitation nowcasting problem. Unlike previous works, at the bottleneck layer, we forecast the future latent embeddings, through a recursive generative process, which are then passed to a decoder. We extend this generative forecasting technique to the skip connections, by appending the recursively generated embeddings from each encoder level with the embeddings at their respective level in the decoding blocks. This allows for improved capturing of features at each decoder level and leads to less information loss due to the pooling operations. The network is trained using global IMERG observations (Huffman et al. 2020), as well as the GFS forecasts (GFS, NCEP 2021), providing key drivers of precipitation in time and space. Beyond the widely used mean-squared error (MSE) loss function that can lead to underestimations of precipitation extremes, we examine the impacts of the focal loss function (FL, Lin et al. 2017). This loss function enables capturing the shape of precipitation distribution through a multi-class representation of precipitation rates beyond second-order penalization of nowcasting error, promising to improve nowcasting of precipitation extremes (Huang et al. 2023).

Section 2 explains the data, preprocessing operations, and the mutual information between the inputs and outputs of GENESIS. The methodology is explained in Section 3 and the results and discussion are presented in Section 4. Section 5 concludes and conjures up future research directions.

## 2. Data, Preprocessing, and Input Feature Analysis

### *a. Data*

As previously noted, the inputs to GENESIS comprise a temporal sequence of IMERG precipitation, along with physically relevant variables from GFS by the National Centers for Environmental Prediction (NCEP, NCEP 2021). The half-hourly (hourly) IMERG (GFS) training data are collected from April 2020 to March 2023. The data over the first two years are used for training and the rest for testing.

The IMERG integrates passive microwave (Kummerow et al. 2015) and infrared (Hong et al. 2004) precipitation from the GPM constellation and geostationary satellites. The passive microwave precipitation is mostly processed by the Goddard PROFiling algorithm (GPROF, Kummerow et al. 2015) and is merged with infrared precipitation (Hong et al. 2004) to fill the temporal gaps, using a Kalman filtering approach (Joyce and Xie 2011). The IMERG product provides gridded precipitation rates globally at  $0.1^\circ$  every 30 minutes. The product is available at three different time latencies: Early Run, Late Run, and Final Run. For this study, sequences of half-hourly Early Run (V06) are used with a minimum time latency.

The NCEP’s GFS constitutes an atmospheric model that is coupled with the Noah land surface model with multi-parameterization options (NoahMP, Niu et al. 2011), the Modular Ocean Model version 6 (MOM6, Adcroft et al. 2019), and the Los Alamos sea ice model (CICE6, Hunke et al. 2017). The GFS atmospheric model uses the Finite Volume Cubed-Sphere Dynamical model (FV3) developed by the Geophysical Fluid Dynamics Laboratory (GFDL, Putman and Lin 2007). In the vertical dimension, there are 127 pressure levels with the top layer centered around 80 km height. The initial conditions are provided through the Global Data Assimilation System (GDAS, Abreu et al. 2012), which ingests various satellite and ground-based observations using a 4-Dimensional system (Lorenc et al. 2015). Here we confine our considerations to the hourly forecasts (v16) of 2-m horizontal ( $U, V$ ) wind velocities in  $\text{m s}^{-1}$  and total precipitable water (TPW,  $\text{kg m}^{-2}$ ) content at resolution  $0.25^\circ$ .

These three physical variables are primarily selected for two main reasons while keeping the computational burden of the training process under control. Firstly, wind velocity plays a pivotal role in the atmospheric transport of moisture and thus the evolution of precipitation cells (Huang et al. 2023; Jin et al. 2023). Secondly, forecasts of TPW identify the temporal evolution of moisture-laden convective clouds and thus potentially improve the predictive skill of the nowcasting machine, especially in relationship with extreme precipitation (Kim et al. 2022).

### *b. Preprocessing for Training*

The question is how many sequences of IMERG are needed to be fed into the nowcasting machine. The answer to this question may be obtained through auto-correlation analysis. Fig. 1 shows the

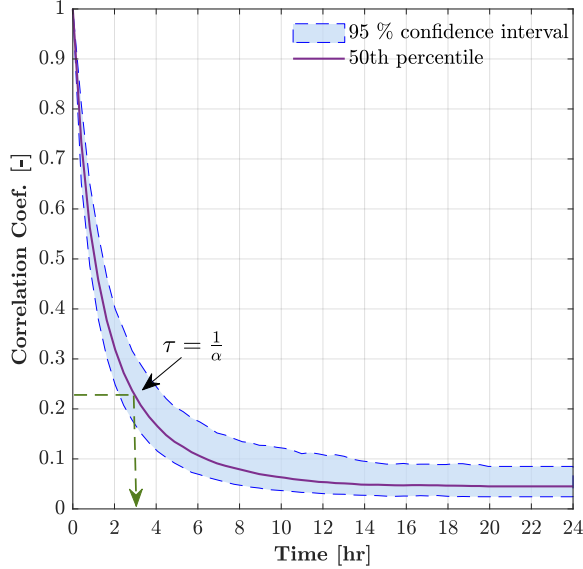


FIG. 1. Correlation coefficients between IMERG precipitation snapshots at different time lags show an exponential decay rate of  $\alpha \approx 0.33 \text{ hr}^{-1}$  and a correlation length  $\tau$  of almost 3 hours.

median and 95% confidence bound of the temporal correlation at different time lags over a 24-hour time window, using 1,000 randomly selected IMERG precipitation snapshots.

The analysis shows that the correlation decays almost exponentially in time with a mean rate of  $\alpha \approx 0.33 \text{ hr}^{-1}$ , equivalent to a correlation length of  $\tau = 1/\alpha \approx 3 \text{ hr}$ . As is evident, after 6 hours, the median of the coefficients is around 0.1 and reaches a plateau of 0.05 after approximately 12 hours. Therefore, it appears that beyond 6 to 8 hours, the global precipitation fields have minimal memory of the past, even though a negligible long-range dependency appears to persist. Given this information and the computational complexity of the problem, we confine our considerations to a time window of six hours for nowcasting the next four hours every 30 minutes.

Mapping the GFS variables to the IMERG grid using the nearest-neighbor interpolation, over each grid of the training data at time  $t$  there is  $C = 4$  number of predictors including IMERG precipitation  $P$ , TPW,  $U$ , and  $V$  – stored in the channel dimension of a tensor array  $X^t \in \mathbb{R}^{M \times N \times C}$ . Unlike IMERG precipitation, GFS forecasts are available on an hourly time scale. Therefore, for twelve past sequences of IMERG, we use six past and future sequences of GFS data and organize them for training (Fig. 2) as follows:

$$\begin{aligned}
X^t &= \left[ P^t | TPW^{(t+12\Delta t)} | U^{(t+12\Delta t)} | V^{(t+12\Delta t)} \right] \\
X^{(t-\Delta t)} &= \left[ P^{(t-\Delta t)} | TPW^{(t+10\Delta t)} | U^{(t+10\Delta t)} | V^{(t+10\Delta t)} \right] \\
&\vdots \\
X^{t-n\Delta t} &= \left[ P^{(t-n\Delta t)} | TPW^{(t+6-2n\Delta t)} | U^{(t+6-2n\Delta t)} | V^{(t+6-2n\Delta t)} \right],
\end{aligned} \tag{1}$$

where  $n = 0, 1, \dots, 11$  with  $\Delta t = \frac{1}{2}$  hr. By stacking multiple tensors over 6 hours, we have the entire training block of input predictors as  $\mathcal{X} = [X^t | X^{t-\Delta t} | \dots | X^{t-11\Delta t}] \in \mathbb{R}^{M \times N \times C \times T}$ . This input block of data is fed into the network to predict the output tensor  $\mathcal{Y} = [P^{t+\Delta t} | P^{t+2\Delta t} | \dots | P^{t+8\Delta t}] \in \mathbb{R}^{M \times N \times T_f}$  that contains the next 4 hours of future IMERG precipitation such that  $\mathcal{Y} = f(\theta, \mathcal{X}) : \mathbb{R}^{M \times N \times C \times T} \rightarrow \mathbb{R}^{M \times N \times T_f}$ , where  $\theta$  denotes all the unknown network parameters.

Here, we choose patches of size  $M = N = 256$  to make the training process computationally amenable. The outputs are then tiled with 50% overlap and only  $128 \times 128$  interior pixels are used to reconstruct the entire domain of IMERG. Overall, 100,000 patches of tensor blocks were randomly sampled over the spatial domain of the problem from April 2020 to March 2022. This data set was split into 70 and 30% for training and validation. For testing 15,000 independent random samples were used from April 2022 to March 2023.

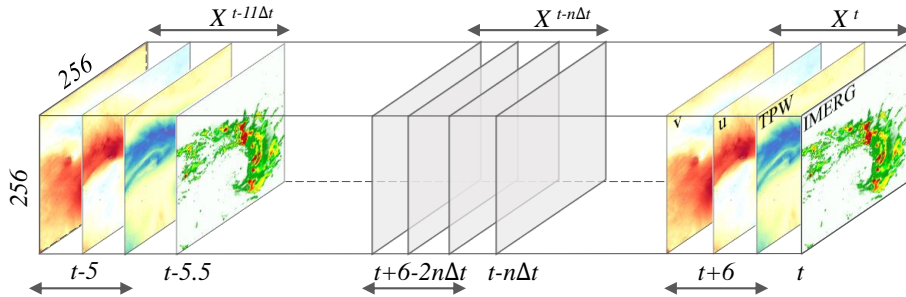


FIG. 2. Schematic of the input tensors  $X^{t-n\Delta t}$  over 6 hours with  $n = 0, \dots, 11$  – organized for training the nowcasting machine with  $\Delta t = 1/2$  hr. The tensors contain past IMERG precipitation as well as past and future GFS data of TPW and near-surface horizontal wind velocities components  $U$  and  $V$ .

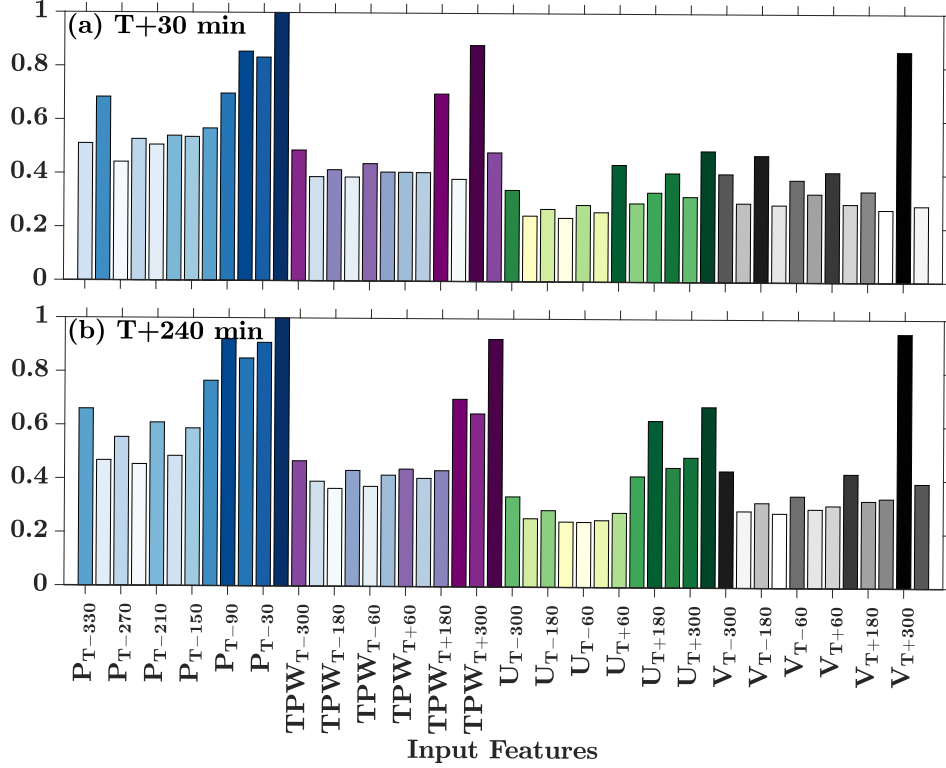


FIG. 3. Minimum redundancy and maximum relevance (MRMR) scores of inputs for precipitation nowcasting at (a) first, and (b) last lead time.

### c. Input Feature Analysis

Before delving into the design of the nowcasting machine, a key question emerges: Amongst the used predictors, what are the most important ones concerning the short-term evolution of precipitation fields? Here, to shed light on this question, the maximum relevance and minimum redundancy method (MRMR, Peng et al. 2005) is employed. This method identifies the most informative and the least redundant features in a given set of predictors, irrespective of the underlying ML algorithm. Specifically, it finds an optimal set  $S$  of features that maximizes  $A_s = 1/|S| \sum_{x \in S} I(x, y)$ , the relevance of features in  $S$  with respect to a response variable  $y$ , and minimizes  $B_s = 1/|S|^2 \sum_{x, z \in S} I(x, z)$ , the redundancy of features in  $S$  – where  $I(\cdot, \cdot)$  is the mutual information and  $|S|$  denotes the cardinality of  $S$ . Those predictors with high MRMR scores exhibit the highest mutual information with the temporal evolution of precipitation fields and the least redundancy in terms of their internal mutual information.

The results of the MRMR analysis at both the initial (a) and final (b) lead times are presented in Fig. 3. The figure illustrates that, at the first lead time, on average, previous precipitation fields exhibit a higher mean score (0.64), followed by TPW (0.48) and horizontal wind velocity (0.32). Within the precipitation sequence, the first 2 hours display a higher MRMR score, and the score gradually decreases as we move backward in time. For the TPW, the future sequences  $T + 150 - T + 300$  min demonstrate the highest scores, highlighting their predictive impacts for longer lead times. Moreover, the scores for  $U$  are larger than  $V$  and increase for longer lead times, as the global storm morphology and evolution are chiefly governed by the prevailing easterlies and westerlies.

Examining the mutual information between inputs and precipitation fields at a 4-hour lead time (Fig. 3-b) reveals that still, previous sequences of precipitation are more important than the used physical variables. However, the mean MRMR score for physical variables shows an increase of 6, 12, and 4% for TPW,  $U$ , and  $V$ , respectively, compared to those for the 30-minute lead time. This further highlights the role of horizontal velocity forecasts in the nowcasting of precipitation for longer lead times.

### 3. Methodology

#### *a. Network Architecture*

The used architecture fuses a U-Net (Ronneberger et al. 2015) and a Convolutional LSTM (ConvLSTM, Shi et al. 2015) neural network. The standard U-Net encodes the semantic information of a single image into a low-dimensional latent representation, which is then decoded to produce the segmentation results along with the help of skip connections. These connections help to recover fine-level details lost in the encoding stage and converge much faster to the optimal estimate of the network parameters while alleviating the vanishing gradient problem (LeCun et al. 2015). However, the U-Net architecture is primarily designed to learn spatial features of static fields and has no specific mechanisms for capturing temporal dependencies in data sequences (Wang et al. 2022).

For time series modeling with temporal dependencies, LSTM networks extend the predictive skills of classic RNNs (Hochreiter and Schmidhuber 1997). The LSTM memory cells enable the retention of important dependencies and propagate the error information over a sufficiently long window of time for updating its parameters without the vanishing and/or exploding gradients

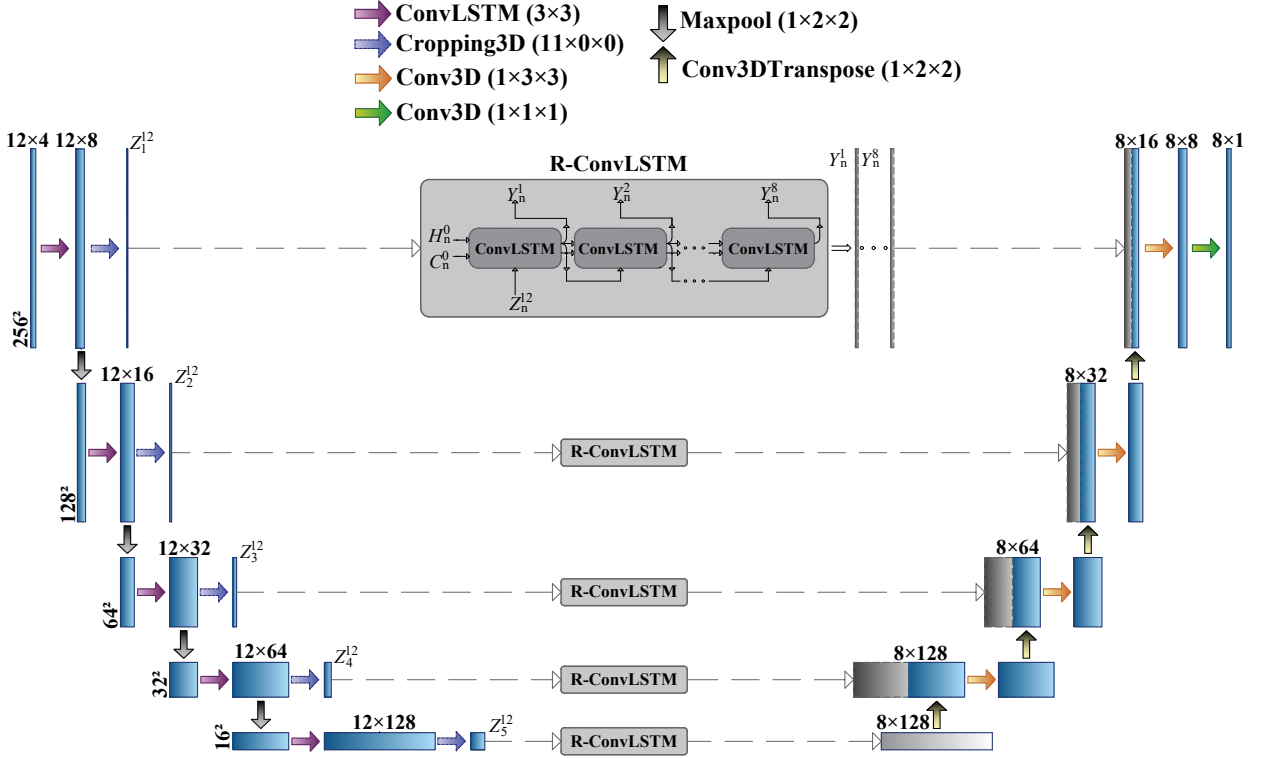


FIG. 4. Schematics of the GENESIS nowcasting machine. An encoder operates over a sequence of input data, at 12 time steps, through a series of convolutional LSTM kernels to extract their low-dimensional spatiotemporal features and then a decoder upsamples the features through a series of deconvolution to reconstruct the evolution of precipitation fields over a 4-hour lead time at 8 time steps.

problems (Hochreiter and Schmidhuber 1997; Graves 2013). However, LSTMs work mainly with time series data, which are not spatial in nature. To overcome this issue, the Convolutional LSTM (ConvLSTM) cell was introduced (Shi et al. 2015) for time series analysis of spatial domains. In the context of precipitation nowcasting, it is important to note that while the dynamics of the involved atmospheric variables may not necessarily exhibit long-range temporal dependencies, it is imperative to deploy modern LSTM networks to account not only for potential long-range dependencies but also the existing short-range correlations.

To harness the combined capabilities of U-Net and ConvLSTM, we propose a new architecture for IMERG precipitation nowcasting (Fig. 4). In the proposed architecture, each input tensor  $X \in \mathbb{R}^{H \times W \times C}$  of a sequence  $\mathcal{X} = [X^1, X^2, \dots, X^T]$ , with  $T = 1, \dots, 12$  is passed through a ConvLSTM operator to encode the spatiotemporal information of each timestep into a latent representation

$Z_n^T \in \mathbb{R}^{H' \times W' \times C'}$  at  $n = 1, \dots, 5$  encoder blocks, followed by max-pooling, batch normalization, and 15% dropout layers.

In the last encoding block, the nowcasting machine passes the latent embeddings of the preceding ConvLSTM  $Z_{n=5}^{12}$  through a Recursive ConvLSTM (R-ConvLSTM) operator that forecasts the evolution of the embeddings over the next 4-hour lead time at eight timesteps. As sketched in Fig. 4, this recursive generative process is also repeated for skip connections at multiple encoding blocks which allows for improved capturing of features at each decoder level and leads to less information loss due to the pooling operations.

The Recursive ConvLSTM uses  $Z_n^{12}$  as input and considers zero values for the initial hidden  $H_n^0$  and cell  $C_n^0$  states to compute the output states  $Y_n = [Y_n^1, \dots, Y_n^T]$  for  $T = 1, \dots, 8$  time steps, recursively. These predicted states are then concatenated with the outputs of a transposed 3D convolution operator (Conv3DTranspose) at each encoder block and passed through a 3D temporal convolution (Conv3D), batch normalization, and 15% dropout layers.

Note, to ensure that the context of the last encoder latent embedding (i.e.  $Z_n^{12}$ ) is not lost while the recursive generation of future latent spaces is happening, we add this final context to each input of the recursive generative process. This technique helps retain the information across all the timestamps of forecast and has been shown to lead to better temporal generation (Ravirathinam et al. 2023). Specifically, at each step of future latent embedding generation, three outputs are given: output features, cell states, and hidden states. The context tensor,  $Z_n^{12}$ , is then added to the output features, to create the joint context. This joint context is passed as input to the next step of the recursive ConvLSTM, with the new cell and hidden states. This process is repeated until the eight steps of future latent embeddings have been created. This creation of the joint context helps preserve information from the encoder over multiple steps of unrolling.

### *b. Loss Functions*

In the proposed architecture, the choice of the loss function can impact the accuracy of precipitation nowcasting. Different loss functions can be tested for this purpose including the mean squared or absolute error losses, Wasserstein distance (Villani et al. 2009), and those loss functions that are often used for classification problems such as the cross entropy (MacKay and Mac Kay 2003) and FL functions (Lin et al. 2017).

Commonly used loss functions such as the MSE cannot capture the non-Gaussian probability distribution of the precipitation fields (Guiloteau et al. 2023; Ehsani et al. 2022). Another approach is to discretize the input-output rates of precipitation into a finite number of intervals and recast the nowcasting into a multi-class classification problem. The main advantage of the latter approach is that the network would attempt to implicitly reconstruct the precipitation histogram rather than minimize the second-order statistics of the nowcasting error (Pfreundschuh et al. 2022).

As a commonly used loss function for classification tasks, cross-entropy measures the dissimilarity between two discrete probability distributions. However, its performance degrades markedly, when there is a high imbalance between the number of classes. In this scenario, those classes with a large number of training samples (i.e., low precipitation rates) will dominate the value of the loss function, causing the weights to be updated in a direction that the network becomes less and less skillful in predictions of those classes with lesser training samples (i.e., high precipitation rates).

To that end, the FL loss function uses a focusing parameter  $\gamma$  to avoid saturating the loss with the impacts of easy-to-classify samples and balances the contribution of each class to the total loss by a weighting factor  $\alpha_c$  as follows:

$$\text{FL}(y, p) = -\frac{1}{N} \sum_{i=1}^N \sum_{c=1}^C \alpha_c y_{i,c} (1 - p_{i,c})^\gamma \log p_{i,c} \quad (2)$$

where  $y_{i,c}$  and  $p_{i,c}$  are the reference and predicted probabilities of  $c^{\text{th}}$  class for  $i = 1, \dots, N$  training data points. The  $\alpha_c$  is proportional to the inverse of the frequency of occurrence of class data points, such that  $\sum_c \alpha_c = 1$ , and  $\gamma$  commonly ranges from 2 to 5, with larger values for highly imbalanced training data sets.

We use both regression MSE and FL loss functions, with  $\gamma = 2$ , for training the nowcasting machine, hereafter often referred to as GENESIS<sub>MSE</sub> and GENESIS<sub>FL</sub>, respectively. To train GENESIS<sub>FL</sub>, the precipitation rates are discretized into 10 classes in a logarithmic scale ranging from 0.1 to 32 mm hr<sup>-1</sup>. Rates below (above) 0.1 (32) mm hr<sup>-1</sup> are assigned to class 1 (10). Note, that the only difference in the architecture of the network when using MSE and FL loss functions, is the final operation in the last decoder block (Fig. 4). This operation employs a layer of 1 × 1 convolution followed by a normalization layer and a ReLU activation (Softmax) for the MSE (FL) loss. It is important to emphasize that the GENESIS<sub>FL</sub> network produces output in the form

of posterior probabilities for classes within each bin. These posterior probabilities serve as the foundation for calculating the maximum a-posteriori estimate of the precipitation class through the Softmax function and can be used to detect the exceedance probability of a precipitation threshold (Pfreundschuh et al. 2022). To obtain the optimal weights of both networks, the Adam optimizer (Kingma and Ba 2014) is employed with an initial learning rate  $\eta=1E-3$  and the mini-batch size 8. A decay factor of 0.1 is set for the learning rate at every 10 epochs when there is no improvement in the validation loss. To initialize the weights of the nowcasting networks, the *Xavier* method (Sun et al. 2014b) is used. The network is trained using the TensorFlow-V2 library (Abadi et al. 2016) on an AMD EPYC 7542 with a 32-core central processing unit and 1008 GB of random access memory – equipped with an NVIDIA A-100 40-GB graphical processing unit, provided by the Minnesota Super Computing Institute (MSI).

### c. Nowcasting Quality Metrics

To assess the quality of precipitation nowcasts, common categorical evaluation metrics are used including precision  $TP/(TP + FP)$ , recall  $TP/(TP + FN)$ , Heidke skill score (HSS, Jolliffe and Stephenson 2012), and critical success index ( $CSI_r$ ,  $TP/(TP + FN + FP)$ , (Schaefer 1990)) – in which the true positive (TP), true negative (TN), false positive (FP), and false negative (FN) rates characterize the confusion matrix. Furthermore, to compare the performance of the models at different spatial scales, fractions skill score  $FSS=1 - \frac{\sum_{i=1}^M (S_f^i - S_{obs}^i)^2}{\sum_{i=1}^M (S_f^i)^2 - \sum_{i=1}^M (S_{obs}^i)^2}$  is used in which  $S_f$  and  $S_{obs}$  are fractional coverage of the nowcasts and observations for  $M$  selected windows with a spatial scale of interest (Ayzel et al. 2020).

To quantify the dissimilarity between the observed and predicted probability distribution of precipitation classes, the Wasserstein distance (Villani et al. 2009) is employed. This metric is derived from optimal transport theory, which considers the problem of quantifying the cost of morphing one distribution into another non-parametrically. The cost defines a distance metric that not only penalizes the shifts between the mean of the distributions (bias) but also the misshape in terms of all higher-order moments. Smaller values of this metric denote that the two densities are closer in terms of their central locations and shapes. For further information, the readers are referred to (Ning et al. 2014; Tamang et al. 2020, 2021) in the context of geophysical data assimilation and climate model comparisons (Robin et al. 2017; Vissio et al. 2020).

The value of precision, recall,  $CSI_r$ , and FSS can vary from 0 to 1 with a perfect score of 1. The values of HSS vary from  $-\infty$  to 1 indicating the worst and the best forecasts while positive values denote better than a random prediction. To compute  $CSI_r$  index, the elements of the confusion matrix are determined for a binary representation of the precipitation fields with the rates above a prespecified threshold rate  $r$  in  $\text{mmhr}^{-1}$ . To evaluate the performance of the regression network using categorical scores, the predicted rates are converted to the same classes defined for the classification network.

#### 4. Results and Discussion

It is important to emphasize that the goal of this section is to demonstrate the extent to which we can predict the sub-hourly evolution of the global precipitation field, considering IMERG as a relative and not an absolute reference observation. Therefore, when the nowcasting results are compared with GFS forecasts, we do not aim to quantify the intrinsic errors between the two data sets. However, the presented results are predicated on the presumption that the observational satellite data exhibit less uncertainty than the GFS predictions.

##### *a. Storm-scale Nowcasting*

Figure 5 shows the nowcasting results of Hurricane Ian initialized at 20:00 UTC on September 27, 2022. Visual inspection indicates that the presented nowcasting machine can predict the storm space-time dynamics. Overall, the GFS predictions are less coherent than IMERG and lack the prediction of some heavy precipitation cells. The extent of the storm in GFS is larger than the IMERG. There are intense precipitation cells in IMERG, organized in the storm band structures, that do not manifest themselves in the GFS forecasts. This is partly expected as the GFS spatial resolution is coarser than IMERG. The difference in capturing high-intense cells is not only apparent over the rainbands around the eyewall but also those extended outer bands, for example near the coasts of South Carolina at the 4<sup>th</sup> time-step. The nowcasting machine seems to produce precipitation fields that are expectedly consistent with the IMERG observations, even though some underestimations are apparent – especially over long lead times due to repeated applications of convolution and max-pooling operations.

Comparing the performance of the GENESIS<sub>MSE</sub> and GENESIS<sub>FL</sub> reveals that at 30 min lead time, both models capture some detailed structures of the observed storm, although the GENESIS<sub>MSE</sub> underestimates the rates, relatively. After an hour, it becomes apparent that the use of the FL function can lead to improved preservation of precipitation extremes when compared to its regression counterpart. It is worth noting that both nowcasts are perceptually closer to the IMERG observations than GFS forecasts. For example, as shown in the dashed red box in Fig. 5 b, an outer rainband manifests itself near the coast of New York and intensifies over longer time steps. This rain band is missed in GFS forecasts; however, is detected and evolved in the nowcasting precipitation products. For longer lead times, the classification network shows a tendency to preserve the precipitation extremes at the expense of overestimating the extent of the storm.

|                  |       | Lead Time |      |      |      |      |      |      |      |
|------------------|-------|-----------|------|------|------|------|------|------|------|
| Metric           | Model | $T+30$    | +60  | +90  | +120 | +150 | +180 | +210 | +240 |
| CSI <sub>1</sub> | GFS   |           | 0.25 |      | 0.25 |      | 0.26 |      | 0.28 |
|                  | MSE   | 0.75      | 0.69 | 0.63 | 0.58 | 0.47 | 0.41 | 0.37 | 0.35 |
|                  | FL    | 0.71      | 0.65 | 0.60 | 0.56 | 0.47 | 0.43 | 0.39 | 0.39 |
|                  | BM    | 0.67      | 0.47 | 0.42 | 0.38 | 0.35 | 0.33 | 0.32 | 0.31 |
| CSI <sub>8</sub> | GFS   |           | 0.14 |      | 0.24 |      | 0.18 |      | 0.12 |
|                  | MSE   | 0.55      | 0.43 | 0.36 | 0.30 | 0.28 | 0.27 | 0.25 | 0.18 |
|                  | FL    | 0.59      | 0.48 | 0.41 | 0.37 | 0.35 | 0.35 | 0.32 | 0.31 |
|                  | BM    | 0.50      | 0.39 | 0.32 | 0.20 | 0.18 | 0.18 | 0.15 | 0.14 |

TABLE 1. Critical success index for GFS, GENESIS<sub>MSE</sub>, and GENESIS<sub>FL</sub> as well as benchmark persistent (BM) scenario against IMERG observations at threshold 1 and 8 mm hr<sup>-1</sup> for the storm shown in Fig. 5.

Table 1 presents CSI<sub>r</sub> with two different rates  $r = 1$  and 8 mm hr<sup>-1</sup> for GFS, GENESIS, and persistence Benchmark (BM) scenario. The persistence BM scenario assumes that the precipitation field remains time-invariant over the nowcasting time steps, commonly used (Ehsani et al. 2022; Ayzel et al. 2020; Agrawal et al. 2019) to test the effectiveness of nowcasting. The results indicate the CSI values for GFS forecasts remain around 0.25 for  $r = 1$  mm hr<sup>-1</sup> and vary between 0.14 to 0.24 for  $r = 8$  mm hr<sup>-1</sup>. For the nowcasting machines, the CSI<sub>1</sub> score decreases approximately from 0.75 to 0.35 when the lead time grows. The CSI<sub>1</sub> score is slightly higher for the GENESIS<sub>MSE</sub> than the GENESIS<sub>FL</sub> over lead times less than 180 minutes and then the GENESIS<sub>FL</sub> gradually

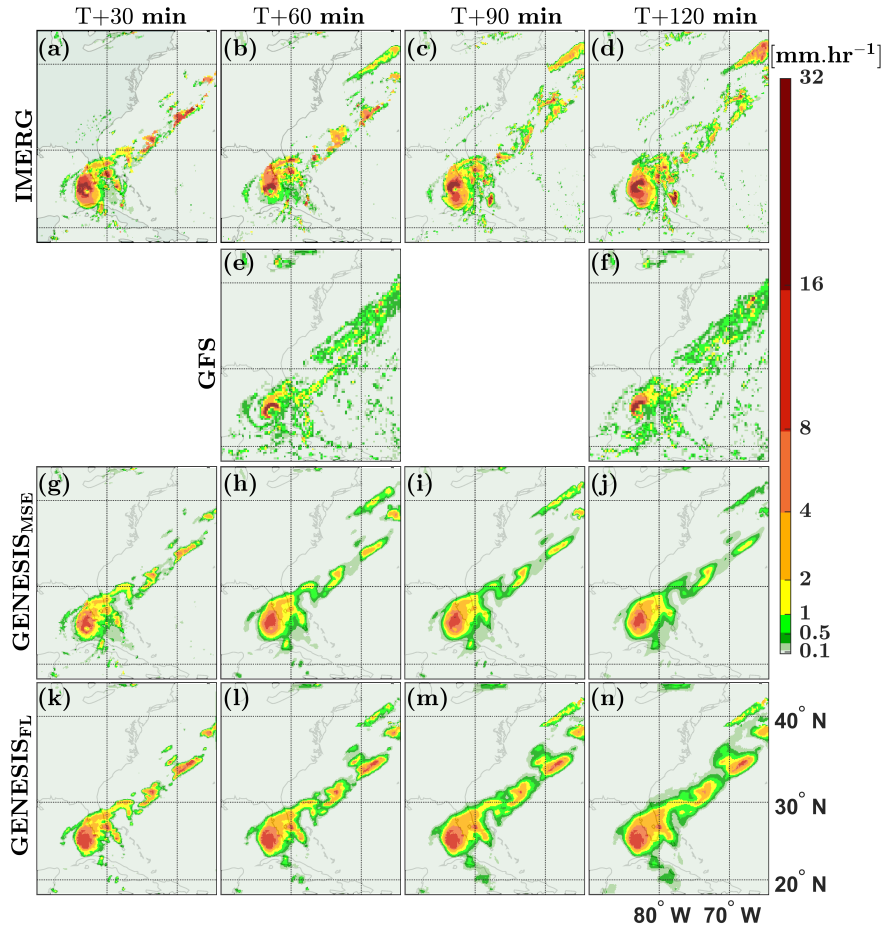


FIG. 5. Evolution of the Hurricane Ian over 2 hours, with a timestep of 30 min, beginning at 20:00 UTC on September 27, 2022, by IMERG (a–d), GFS (e–f), GENESIS<sub>MSE</sub> (g–j), and GENESIS<sub>FL</sub> (k–n).

overtakes the GENESIS<sub>MSE</sub> for longer times. Comparing the performance of GENESIS models with the BM scenario shows that both models outperform it by at least 6% in the first lead time which increases to 42% at the third time step, in terms of the CSI<sub>1</sub> metric. For  $r = 8 \text{ mm hr}^{-1}$ , GENESIS<sub>FL</sub> provides a superior nowcast quality than GENESIS<sub>MSE</sub>, and the difference tends to grow from 8 to 23% as the lead time increases from 30 minutes to 2 hours. The CSI value for the BM scenario is lower than the GENESIS<sub>MSE</sub> models by 10% and 28% at the first and last lead times, which is expected given that the intensity and morphology of high-intense precipitation cells evolve faster in time than those cells with lighter rates.

An important outcome of GENESIS<sub>FL</sub> is that it can provide the class probability through the Softmax layer and thus the exceedance probabilities. Figure 6 a–d shows the storm (first row) over

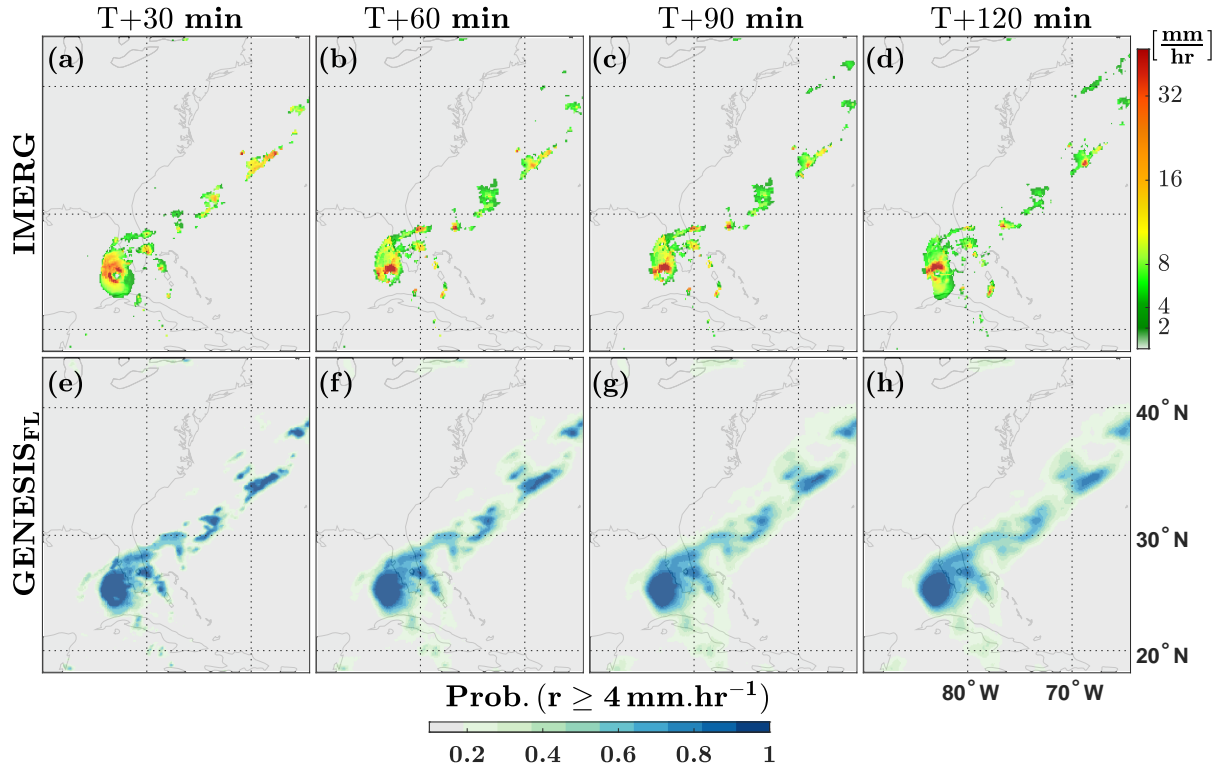


FIG. 6. Evolution of the Hurricane Ian over 2 hours beginning at 20:00 UTC on September 27, 2022, by IMERG (a–d) masked for the rates above  $4 \text{ mm hr}^{-1}$ , and the corresponding probability of exceedance using GENESIS<sub>FL</sub> (e–h).

the areas with rates greater than  $4 \text{ mm hr}^{-1}$  and the associated exceedance probabilities (second row). The results show the capability of GENESIS<sub>FL</sub> in capturing the shape of intense precipitation with high probability. As the lead time increases, the predictions become increasingly blurry, which manifests itself in the probability maps as well.

### *b. Multi-storm Nowcasting*

To provide a more comprehensive evaluation of the nowcasting machines, we randomly selected 15,000 independent samples of input-output tensor blocks, from April 2022 to March 2023 and used them for nowcasting and calculation of the forecast quality metrics. Four different metrics including  $\text{CSI}_T$  at three threshold values, precision, recall, and HSS are calculated for each sample, and their ensemble mean is presented in Fig. 7 for different lead times.

Figure 7 a shows the  $CSI_1$  for all three nowcasts and the BM scenario. The GFS performance is fairly stable over different lead times and remains around 0.3. However,  $CSI_1$  for regression (classification) network reduces from 0.65 to 0.42 (0.58 to 0.35) when lead time increases from 30 to 240 min. This difference can be attributed to the imbalanced nature of the data and improved skills of the regression network to represent the bulk of the precipitation distribution. Both GENESIS models outperform the persistence BM scenario, for which  $CSI_1 = 0.54$  at 30 min and declines rapidly by a factor of 2 at 240 min lead time.

By increasing the CSI threshold to  $4 \text{ mm hr}^{-1}$  (Fig. 7 b), the performance of GFS forecasts reduces by 30%, from 0.30 to 0.20, at  $T + 60$  min but still remains fairly invariant in time. However, the performance of the regression network decays by a factor of 2, from approximately 0.53 to 0.23, when lead time increases from half an hour to four hours. Meanwhile, the  $CSI_4$  in the classification network decays from 0.56 at 30 min to 0.28 at 240 min, showing that this network begins to outperform the regression network by capturing higher intensity precipitation rates.

For more intense precipitation (Fig. 7 c), the results indicate that the value of  $CSI_8$  at the second lead time for GFS,  $GENESIS_{MSE}$ ,  $GENESIS_{FL}$ , and BM models decay by 65, 27, 25, and 30% at  $T + 60$  min compare to  $CSI_4$ , respectively. This metric, for the regression network, has its highest value of 0.39 at 30 min lead time and reduces to 0.1 after three hours. Meanwhile, the classification network still shows some skills and a potential to accurately capture precipitation rates above 8

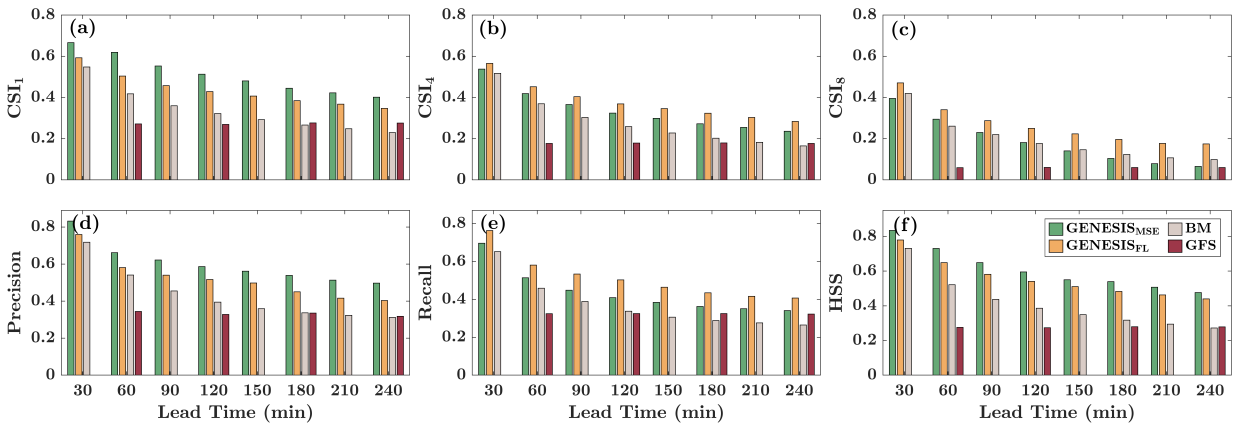


FIG. 7. Ensemble mean of (a)  $CSI_1$ , (b)  $CSI_4$ , (c)  $CSI_8$ , (d) precision, (e) recall, and (f) HSS for  $GENESIS_{MSE}$ ,  $GENESIS_{FL}$ , GFS forecasts, and BM scenario using 15,000 independent input samples from the test set.

$\text{mm hr}^{-1}$ , as  $\text{CSI}_8$  is around 0.47 (0.17) at 30 (240) min. It should be noted that the  $\text{CSI}_8$  is low for all predictions and never exceeds 0.4 for the regression network.

Figure 7 d shows the mean precision metric, which explains the number of truly detected precipitating events divided by all detected precipitating events. The precision value for GFS remains constant in time around 0.35. For the regression (classification) network, it is around 0.83 (0.76) at the first lead time and decays by 30 (32)% to 0.58 (51) at the fourth time step and then remains relatively constant for longer times. The reason can be attributed to the fact that while the classification network has a higher probability of detection than the regression network, it also exhibits a higher false alarm rate, especially in capturing the more frequent body of precipitation distribution with a rate of less than  $1\text{--}1.5 \text{ mm hr}^{-1}$ . The elevated number of false alarm rates leads to a larger denominator in the precision equation, resulting in lower values. As shown, the precision improves over longer lead times relative to the BM scenarios, and the  $\text{GENESIS}_{\text{MSE}}$  consistently outperforms other nowcasts.

The recall metric (Fig. 7 e) shows the ratio of correctly classified sample points to the total observations. The recall value of GFS forecasts is around 0.35 and remains invariant in time. The regression network has a value equal to 0.69 at the first time step which reduces by a factor of 2 at the fifth lead time and remains relatively constant around 0.35. Meanwhile, the metric for the classification network is around 0.75 (0.50) at 30 (150) min. The reason can be attributed to the higher skills of this network in detecting high-intense precipitation rates with low false negatives. As for the BM approach, the recall is close to  $\text{GENESIS}_{\text{MSE}}$  at the first time step but drops by a factor of 1.5 to 0.45, at the next time step. Regarding HSS (Fig. 7 f), the GFS forecasts show a time-invariant HSS of around 0.30. Both regression and classification networks have high values of around 0.80 at 30 min, which are reduced to 0.47 and 0.44 at 240 min, respectively.

Lastly, we compared the results of  $\text{GENESIS}$  with a simple random forest (RF) ML model that operates at the pixel level and does not account for the spatiotemporal evolution of the input data. The RF model was configured with a maximum depth of 10 with 20 ensemble decision trees. The results show a significantly lower performance in terms of all the evaluated quality metrics (not shown here). As an example, the  $\text{GENESIS}$  outperforms RF for  $\text{CSI}_1$  and  $\text{CSI}_8$  by a factor of 1.2 (1.1) and 1.7 (2.5) when MSE (FL) is used as a training loss function.

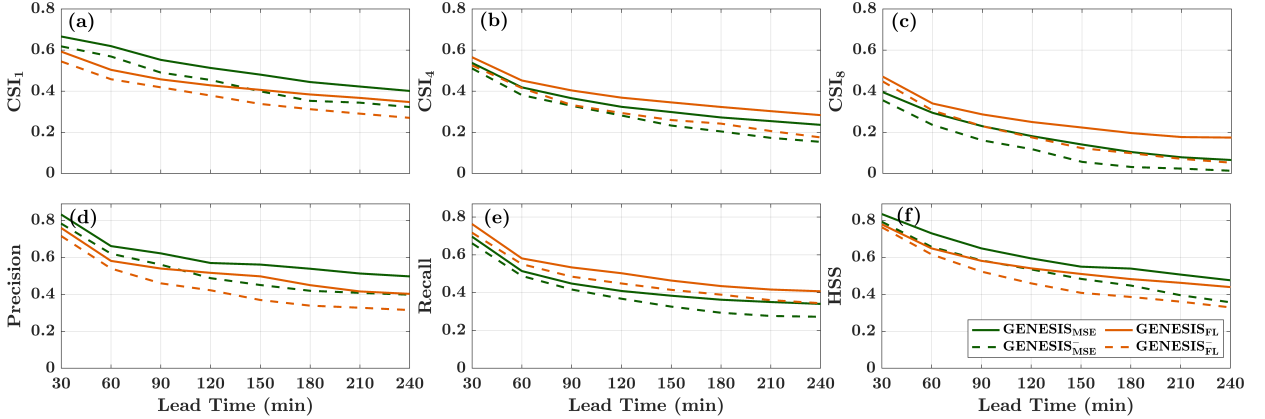


FIG. 8. Ensemble mean of (a) CSI<sub>1</sub>, (b) CSI<sub>4</sub>, (c) CSI<sub>8</sub>, (d) precision, (e) recall, and (f) HSS for 15,000 independent samples from the test set for GENESIS<sub>MSE</sub> and GENESIS<sub>FL</sub> with (solid lines) and without (dashed lines) inclusion of GFS physical variables in the training process.

### c. Impacts of Physical Variables

To quantify the impacts of forecast variables on the performance of the nowcasting machines, we trained identical networks using only sequences of IMERG precipitation (denoted as GENESIS<sup>-</sup>) and compared the outputs with those that are informed by the GFS forecasts as well, using both MSE and FL loss functions.

Figure 8 a shows variation of CSI<sub>1</sub> over a 4-hour lead time. It can be seen that adding the information content of the GFS physical variables improves the nowcasting skill of the regression (classification) models for  $> 1 \text{ mmhr}^{-1}$  by 8 (10)% at  $T + 30$  and by 24 (25)% at  $T + 240$  min. However, at higher CSI thresholds of 4 and 8  $\text{mmhr}^{-1}$  (Fig. 8 b–c), the gains become more significant, which is consistent with the results presented in Fig. 3, concerning the importance of input features.

Figure 8 b, shows that for both GENESIS networks at 30 min lead times, the CSI<sub>4</sub> value without and with GFS inputs are approximately close to each other; however, the difference increases to almost 0.1 after 4 hours. The effects of using physical variables become more pronounced in predicting more intense precipitation at longer lead times (Fig. 8 c) as in the regression (classification) network, the CSI<sub>8</sub> increases from 0.03 to 0.06 (0.02 to 0.11) after 4 hours. Additionally, it is evident that without the inclusion of physical variables, the regression network does not have any

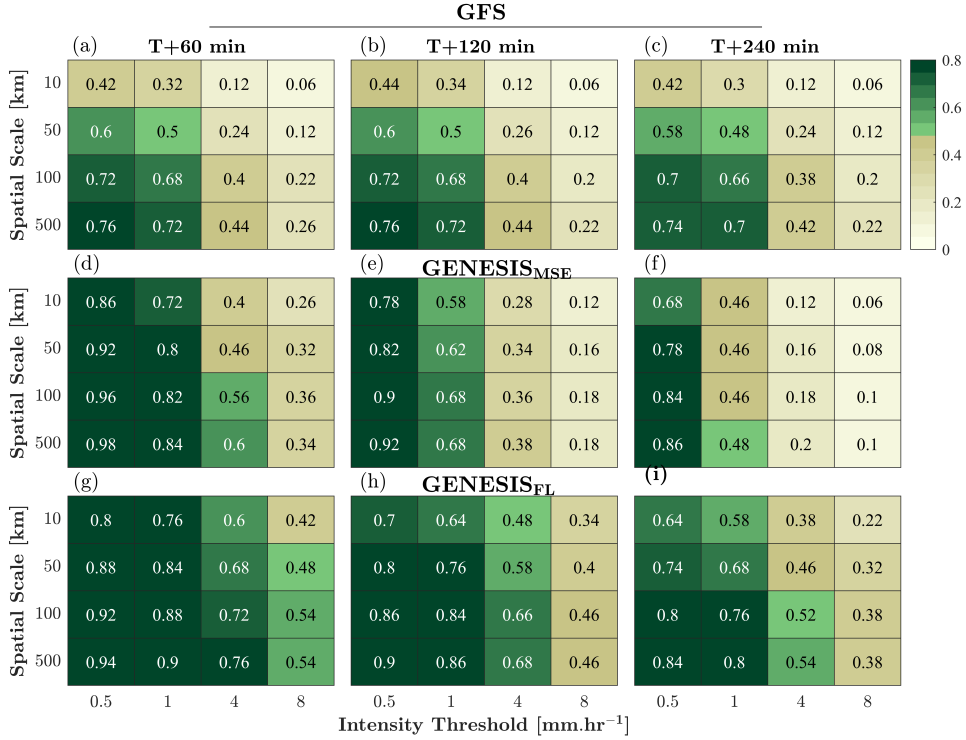


FIG. 9. Fractions skill scores (FSS) for GFS (a–c), GENESIS<sub>MSE</sub> (d–f), and GENESIS<sub>FL</sub> (g–i) at 60, 120, and 240-minute lead times over spatial window sizes of 10, 50, 100, and 500 km for intensity thresholds of 0.5, 1, 4, and 8 mm hr<sup>-1</sup>.

skill in predicting high-intensity precipitation after 180 min while the physically informed network has CSI<sub>8</sub> value around 0.1 at that lead time.

Figure 8 d shows that the inclusion of physical variables in the regression (classification) network causes precision to increase by 6 (8)% at the first and by 22 (29)% at the last time-step. The improvement in recall (Fig. 8 e) for the regression (classification) network grows by 19 (10)% when the lead time increases from 30 to 240 min. In terms of the HSS metric (Fig. 8 f), the same pattern is observed showing that utilizing physical variables can improve the nowcasting skill by around 10% over longer lead times.

#### d. Multiscale Analysis

In this subsection, we aim to use FSS to provide further insights into the dependency of the nowcasting skills on both spatial scales and a precipitation exceedance threshold. As previously explained, this score is obtained by comparing the predicted and reference fractional coverage of

precipitation rates, above a certain threshold, within a spatial window defined by a particular scale. The values greater than  $0.5 + f/2$  are commonly considered skillful, where  $f$  is the fraction of the precipitating area over the analyzed domain (Skok and Roberts 2016). Thus if  $f$  tends to zero, a value of 0.5 can be considered as a lower bound (Mittermaier and Roberts 2010). Figure 9 shows the mean FSS values for GFS, GENESIS<sub>MSE</sub>, and GENESIS<sub>FL</sub>, obtained over 15,000 independent randomly sampled test events.

As expected, the FSS skills drop with decreasing spatial scales, increasing lead times, and increasing intensity thresholds. As shown in Fig. 9 a–c, once again, the GFS skill is not significantly a function of lead time and remains skillful only for intensity threshold of 0.5 and 1 mm hr<sup>-1</sup> at scales greater than 50 km. Note that at these intensity thresholds, the main body of the precipitation distribution is dominated by light values which are easier to capture. By increasing the scale from 50 to 500 km, the skillful FSS values increase roughly from 0.5 to 0.7 across the examined lead times. As expected, the GFS does not show any skill at the native IMERG resolution of 10 km.

Figures 9 d–f indicate that the regression network remains skillful at the native IMERG resolution 10 km when the intensity threshold is 1 (0.5) mm hr<sup>-1</sup> at a 2-hour (4-hour) lead time. However, its performance gradually decreases and becomes closer or even less than GFS for heavier precipitation and longer times. For example, at a scale of 50 km and rates >4 mm hr<sup>-1</sup>, the GFS exhibits a skill of 0.24; however, the skill of the regression network is around 0.16.

The classification network outperforms the GFS and regression network as the rates increase and the scales decrease (Fig. 9 g–i). We can observe that the FSS ranges from 0.58 to 0.68 for rates greater than 4 mm hr<sup>-1</sup> at a 2-hour lead time, across scales 50–500 km, while both GFS and the regression network are not skillful. This observation further highlights that the FL-loss function improves the representation of high-intensity precipitation rates at different scales.

### *e. Global Error Analysis*

This section aims to further evaluate the performance of the nowcasting networks by conducting a quasi-global assessment using the CSI index over one year of the test data, from April 2022 to March 2023. We can provide 48 sets of input tensor blocks (Fig. 2) to the nowcasting machines per day. To make the global analysis computationally amenable and reduce the temporal correlation between the samples, we only confine our considerations to six sampled tensor blocks per day with

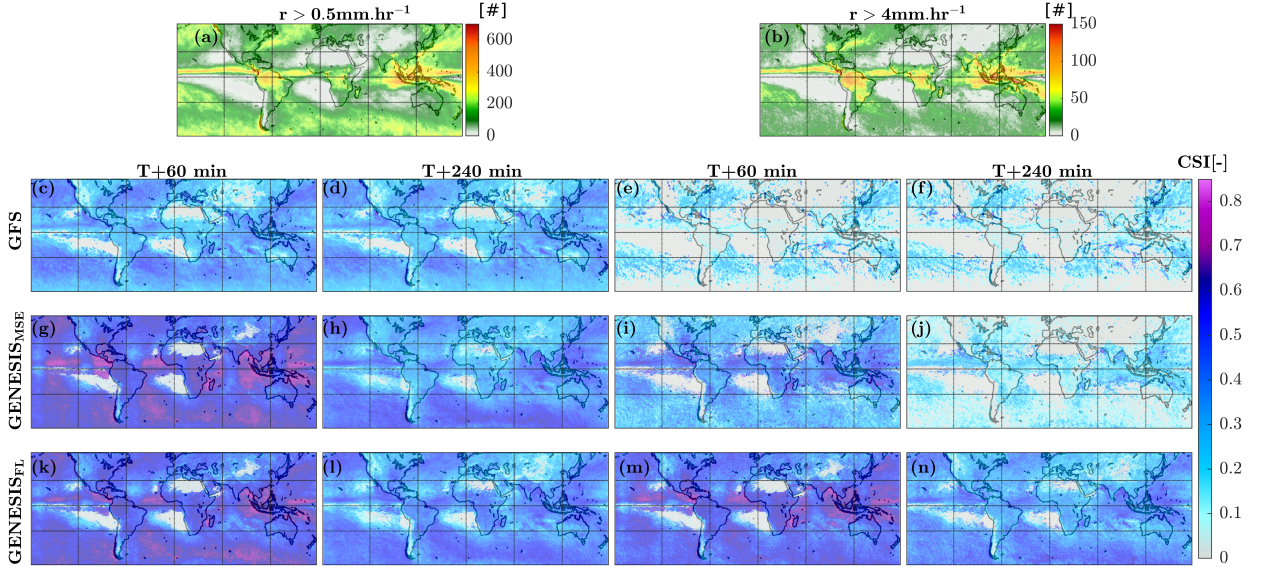


FIG. 10. Occurrence of precipitation rate above 0.5 and 4  $\text{mm hr}^{-1}$  (a–b) along with the associated CSI values at 1 and 4 hour lead times for GFS (c–f), GENESIS<sub>MSE</sub> (g–j), and GENESIS<sub>FL</sub> (k–n).

a 4-hour interval. For comparing the results with the reference IMERG, we use the CSI at two different thresholds 0.5 and 4  $\text{mm hr}^{-1}$  as shown in Fig. 10. To ease the discussion, the CSI values are referred to as high ( $\text{CSI} \geq 0.50$ ), medium ( $0.25 \leq \text{CSI} < 0.50$ ), and low ( $\text{CSI} < 0.25$ ).

Figures 10 a–b show the number of precipitation occurrences with rates greater than 0.5 and 4  $\text{mm hr}^{-1}$ . Precipitation with intensity greater than 0.5  $\text{mm hr}^{-1}$  follows the general global pattern of precipitation occurrence with the highest rates over the Intertropical Convergence Zone (ITCZ), Amazon, and Congo rainforests, as well as the Maritime Continent, where synoptic low-level convergence is the main lifting mechanism (Feng et al. 2021). Over the mid-latitudes, frequent precipitation mainly occurs over the east coast of North America, East Asia, and the Southern Ocean, where frontal lifting often drives the precipitation (Catto et al. 2012). As shown, the occurrence of precipitation with intensity greater than 4  $\text{mm hr}^{-1}$  is more frequent over the tropical regions within  $20^\circ$  S–N, where deep convective precipitation is the predominant regime (Liu et al. 2013).

The  $\text{CSI}_{0.5}$  values for lead times less than 1-hour (Fig. 10 c–d) show that the GFS exhibits low (0.25) and medium (0.35) skills in capturing a large portion of the entire body of the precipitation distribution over land and oceans, respectively. However, by increasing the threshold to 4  $\text{mm hr}^{-1}$ ,

the GFS skill in capturing localized and short-lived precipitation over land decreases significantly to almost zero (Fig. 10 e–f). On the other hand, GFS shows slightly improved CSI<sub>4</sub> over mid-latitudes (0.15) where the extratropical cyclones and their embedded mesoscale frontal sub-systems occur frequently over the Southern Ocean, east coast of North America, and East Asia.

The skill of GFS seems negligible near ITCZ. This may be caused by the misrepresentation of the position of frequent deep and small-scale convective events associated with high-level cumuliform clouds. These clouds are deep and vertically active but small and patchy with a short life cycle of typically less than 2 hr (Rosenfeld and Lensky 1998). These characteristics make prediction of precipitation events location sensitive (Wallace and Hobbs 2006; Zhang and Wang 2021). Analogous to the previous analyses, the results show that the skill is not significantly a function of lead times.

The results in Fig. 10 g–j demonstrate that the regression network has high skills in capturing precipitation rates greater than  $0.5 \text{ mm hr}^{-1}$  both over ocean and land within a 1-hour lead time with mean CSI values of 0.70 and 0.63, respectively. However, the forecast quality declines to medium when the lead time increases by three hours. The regression network, for a  $4 \text{ mm hr}^{-1}$  threshold and a 1-hour lead time, shows high skills over the tropics (0.55) and medium skill over middle latitudes (0.32). Moreover, it can be seen that the skill is higher over the ocean than overland with mean CSI<sub>4</sub> values of 0.63 and 0.50, respectively. This pattern may be attributed to a more localized, intense, and transient nature of overland convective precipitation. Increasing the lead time to 4 hours, the regression network shows almost negligible skills over the middle latitudes, where nimbostratus clouds produce relatively long-lived storm events. The skill becomes low (i.e., CSI<sub>4</sub>  $\approx$  0.15) over the tropics, where mostly cumulonimbus clouds produce frequent intense convective precipitation (Houze Jr 2014).

Figure 10 k–n indicate that GENESIS<sub>FL</sub> has approximately similar skill in capturing precipitation rate greater than  $0.5 \text{ mm hr}^{-1}$  compared to GENESIS<sub>MSE</sub>. However, it has high skills for  $4 \text{ mm hr}^{-1}$  threshold at a 1-hour lead time both over the tropics (0.63) and mid-latitudes (0.55). Although, by increasing the lead time to 4 hours, the skill of the classification network decreases to 0.40 and 0.25 over the tropics and mid-latitudes, it still shows a higher skill compared with the regression network in capturing heavier precipitation over both ITCZ and middle latitudes.

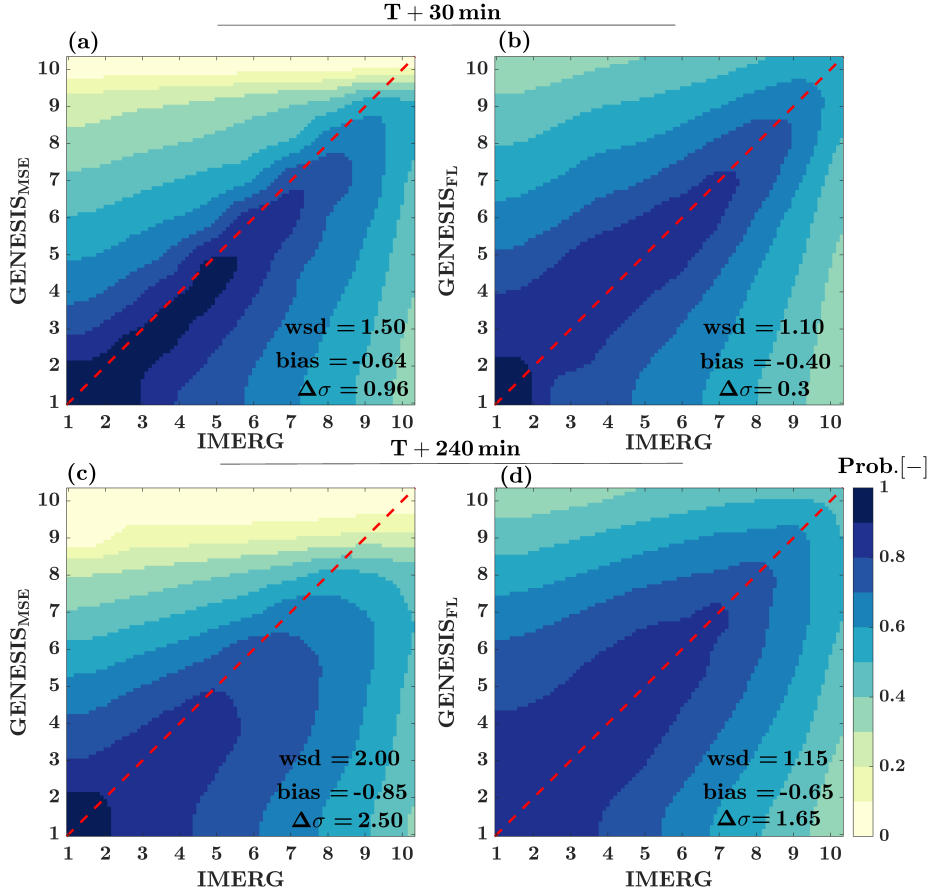


FIG. 11. Scaled joint precipitation class distribution of  $\text{GENESIS}_{\text{MSE}}$  and  $\text{GENESIS}_{\text{FL}}$  in relation to IMERG at 30 (a–b) and 240 min (c–d) lead times. Ten classes are defined in a logarithmic scale ranging from 0.1 to 32  $\text{mm hr}^{-1}$ , assigning rates below (above) 0.1 (32)  $\text{mm hr}^{-1}$  to class 1 (10).

To gain deeper insights into the performance of the nowcasting machines, we examine the joint precipitation class distribution of the nowcasts and IMERG at the first and final lead times. This analysis is conducted using one year of test data, and the results are visualized in Fig. 11. To construct this joint histogram, the continuous precipitation rate obtained from IMERG and the regression network are discretized into the defined classes for one-to-one comparisons. To compare the two discrete distributions, three metrics including the conditional bias for precipitation pixels, the difference in standard deviation ( $\Delta\sigma$ ), and the Wasserstein distance (wsd) are reported.

Visual inspection of Fig. 11 a,b shows that the regression network approximates the IMERG data well in the first four classes with a corresponding precipitation rate below  $1.6 \text{ mm hr}^{-1}$  while

the classification network has overestimation in those ranges. However, for classes with higher precipitation rates; predictions of the classification network are more consistent with the IMERG. The reported metrics reaffirm the improved performance of the classification compared with the regression network. Overall, the classification network demonstrates less underestimation (i.e., bias =  $-0.4 \text{ mm hr}^{-1}$ ) and a closer variability to the IMERG, compared to the regression network (i.e., bias =  $-0.64 \text{ mm hr}^{-1}$ ). Lower values of the Wasserstein distance also indicate that beyond the bias and variability, the classification network is more capable of recovering the entire shape of the precipitation distribution.

Increasing the lead time to 4 hours (Fig. 11 c,d) results in increased dispersion of joint histogram around the diagonal line for both nowcasting networks, which can be attributed to the blurriness effects of the convolution operator at higher lead times. Nonetheless, the classification network continues to outperform the regression network in capturing precipitation at higher rates. As the lead time increases to 4 hours, the Wasserstein distance from the IMERG increases by 33 (5)% for  $\text{GENESIS}_{\text{MSE}}$  ( $\text{GENESIS}_{\text{FL}}$ ).

## 5. Summary and Conclusion

In this paper, we developed the Global prEciPitation Nowcasting using intEgrated multi-Satellite retrIevalS (GENESIS) through a deep autoencoder neural network by fusing Convolutional LSTM into the U-Net architecture. Dynamic skip connections were proposed to predict the evolution of precipitation fields in time using the recursive generative process ConvLSTM at different encoding blocks. It was demonstrated that the architecture can learn efficiently from the past sequences of IMERG precipitation along with past-to-future sequences of physically related variables to predict precipitation globally every 30 minutes within a 4-hour lead time. The developed network was trained using two different loss functions including mean-squared error (regression) and focal loss (classification) to analyze their effects on capturing extreme precipitation events. The performance of the developed models was assessed against GFS nowcasts – considering the IMERG as a relative reference.

The results indicated that recasting the precipitation nowcasting as a classification problem using the FL function can improve capturing the evolution of extreme events beyond a regression loss that relies on the MSE. In particular, on average, the  $\text{CSI}_8$  index increases from 0.18 (regression)

to 0.30 (classification) over the entire 4 hours of lead times for the test data set. In contrast, the regression network showed improved detection of rates greater than  $1 \text{ mm hr}^{-1}$ , which are mainly dominated by less intense precipitation. This finding was further substantiated with joint histogram analysis and computing the Wasserstein distance between the precipitation nowcasts and IMERG. In particular, it was shown that the FL loss function better preserves the shape of the precipitation distribution than the mean squared loss function as the lead time grows.

It was unveiled that, on average, the inclusion of the physical variables in the training, including total precipitable water and horizontal near-surface wind velocities, can improve precipitation nowcasting. For example, the recall rate was increased by 12 (10)% on average over a 4-hour lead time in the regression (classification) network. This improvement was enhanced from 5 (7)% to 25 (17)% as the lead time increased from 30 minutes to 4 hours.

Multiscale analysis of the nowcasting models demonstrated that GFS forecasts were spatially skillful for predicting precipitation rates above  $1 \text{ mm hr}^{-1}$  on spatial scales  $s \geq 50 \text{ km}$ , while the nowcasting machines were capable of capturing those events at the native resolution of IMERG at 10 km within the 2-hour lead time. It was shown that the classification network remains skillful for intensities greater than 1 (4)  $\text{mm hr}^{-1}$  at scales larger than 10 (50) km over the entire 4-hour lead times. Also, the spatial error analysis revealed that, compared to the GFS forecasts, the nowcasting machines seem to be effective in extending short-term forecasts of tropical (convective) precipitation more than mid-latitude (frontal) events.

The following future research directions can be envisaged. First, it will be worth investigating how the inclusion of other forecast variables such as cloud liquid and ice water content, as well as surface soil moisture and temperature, can affect the quality of regional precipitation nowcasting. Second, efforts are needed to be devoted to improving the prediction of heavy precipitation at longer lead times perhaps by providing more high-resolution simulation/observational constraints as well as exploring new loss functions that are more adapted to the problem at hand. Third, increasing the number of classes in the classification network to enhance the accuracy of rate range estimation should be considered for future research. Fourth, it will be worth analyzing the performance of training two separate networks for tropical and mid-latitude regions as this may lead to improvements due to contrasting precipitation regimes in these regions. Lastly, to cope

with the blurriness effects, one might explore embedding a super-resolution convolutional neural network into the nowcasting machine.

This paper is supported with the corresponding repository on GitHub ([https://github.com/reyhaneh-92/GENESIS\\_Nowcast](https://github.com/reyhaneh-92/GENESIS_Nowcast)), which holds pre-trained GENESIS models and architecture – developed in the Python 3 programming language using the Keras deep learning library.

*Acknowledgments.* The first and second authors acknowledge the support from NASA’s Remote Sensing Theory program (RST, 80NSSC20K1717), Making Earth System Data Records for Use in Research (MEaSUREs, 80NSSC24M0048) and Global Precipitation Measurement (PMM, 80NSSC22K0596). The third author also acknowledges the support of the NASA Precipitation Measurement Mission program (PMM, 80NSSC22K0594). Moreover, the authors acknowledge the Minnesota Supercomputing Institute (MSI) at the University of Minnesota for providing resources that contributed to the research results reported in this paper (<https://www.msi.umn.edu/>).

*Data availability statement.* All the utilized datasets are publicly available. The IMERG and GFS datasets can be downloaded from <https://disc.gsfc.nasa.gov/>, and <https://noaa-gfs-bdp-pds.s3.amazonaws.com/index.html#gfs.20220101/00/atmos/>, respectively.

## References

- Abadi, M., and Coauthors, 2016: Tensorflow: Large-scale machine learning on heterogeneous distributed systems. *arXiv preprint arXiv:1603.04467*.
- Abreu, P., and Coauthors, 2012: Description of atmospheric conditions at the Pierre Auger Observatory using the global data assimilation system (GDAS). *Astroparticle Physics*, **35** (9), 591–607.
- Adcroft, A., and Coauthors, 2019: The GFDL global ocean and sea ice model OM4. 0: Model description and simulation features. *Journal of Advances in Modeling Earth Systems*, **11** (10), 3167–3211.
- Agrawal, S., L. Barrington, C. Bromberg, J. Burge, C. Gazen, and J. Hickey, 2019: Machine learning for precipitation nowcasting from radar images. *arXiv preprint arXiv:1912.12132*.
- Austin, G., and A. Bellon, 1974: The use of digital weather radar records for short-term precipitation forecasting. *Quarterly Journal of the Royal Meteorological Society*, **100** (426), 658–664.
- Ayzel, G., M. Heistermann, and T. Winterrath, 2019: Optical flow models as an open benchmark for radar-based precipitation nowcasting (rainymotion v0. 1). *Geoscientific Model Development*, **12** (4), 1387–1402.
- Ayzel, G., T. Scheffer, and M. Heistermann, 2020: RainNet v1. 0: a convolutional neural network for radar-based precipitation nowcasting. *Geoscientific Model Development*, **13** (6), 2631–2644.
- Ban, N., J. Schmidli, and C. Schär, 2014: Evaluation of the convection-resolving regional climate modeling approach in decade-long simulations. *Journal of Geophysical Research: Atmospheres*, **119** (13), 7889–7907.
- Barker, D. M., W. Huang, Y.-R. Guo, A. Bourgeois, and Q. Xiao, 2004: A three-dimensional variational data assimilation system for MM5: Implementation and initial results. *Monthly Weather Review*, **132** (4), 897–914.
- Bowler, N. E., C. E. Pierce, and A. Seed, 2004: Development of a precipitation nowcasting algorithm based upon optical flow techniques. *Journal of Hydrology*, **288** (1-2), 74–91.

- Bowler, N. E., C. E. Pierce, and A. W. Seed, 2006: STEPS: A probabilistic precipitation forecasting scheme which merges an extrapolation nowcast with downscaled NWP. *Quarterly Journal of the Royal Meteorological Society: A journal of the atmospheric sciences, applied meteorology and physical oceanography*, **132 (620)**, 2127–2155.
- Buehner, M., and D. Jacques, 2020: Non-Gaussian deterministic assimilation of radar-derived precipitation accumulations. *Monthly Weather Review*, **148 (2)**, 783–808.
- Catto, J., C. Jakob, G. Berry, and N. Nicholls, 2012: Relating global precipitation to atmospheric fronts. *Geophysical Research Letters*, **39 (10)**.
- Ehsani, M. R., A. Zarei, H. V. Gupta, K. Barnard, E. Lyons, and A. Behrangi, 2022: NowCasting-Nets: Representation Learning to Mitigate Latency Gap of Satellite Precipitation Products Using Convolutional and Recurrent Neural Networks. *IEEE Transactions on Geoscience and Remote Sensing*, **60**, 1–21.
- Errico, R. M., P. Bauer, and J.-F. Mahfouf, 2007: Issues regarding the assimilation of cloud and precipitation data. *Journal of the Atmospheric Sciences*, **64 (11)**, 3785–3798.
- Feng, Z., and Coauthors, 2021: A global high-resolution mesoscale convective system database using satellite-derived cloud tops, surface precipitation, and tracking. *Journal of Geophysical Research: Atmospheres*, **126 (8)**, e2020JD034202.
- Germann, U., and I. Zawadzki, 2002: Scale-dependence of the predictability of precipitation from continental radar images. Part I: Description of the methodology. *Monthly Weather Review*, **130 (12)**, 2859–2873.
- Graves, A., 2013: Generating sequences with recurrent neural networks. *arXiv preprint arXiv:1308.0850*.
- Guilloteau, C., P. V. Le, and E. Foufoula-Georgiou, 2023: Constraining the multiscale structure of geophysical fields in machine-learning: the case of precipitation. *IEEE Geoscience and Remote Sensing Letters*.
- Han, L., H. Liang, H. Chen, W. Zhang, and Y. Ge, 2021: Convective precipitation nowcasting using U-Net Model. *IEEE Transactions on Geoscience and Remote Sensing*, **60**, 1–8.

- Hochreiter, S., and J. Schmidhuber, 1997: Long short-term memory. *Neural computation*, **9** (8), 1735–1780.
- Hohenegger, C., P. Brockhaus, C. S. Bretherton, and C. Schär, 2009: The soil moisture–precipitation feedback in simulations with explicit and parameterized convection. *Journal of Climate*, **22** (19), 5003–5020.
- Hong, Y., K.-L. Hsu, S. Sorooshian, and X. Gao, 2004: Precipitation estimation from remotely sensed imagery using an artificial neural network cloud classification system. *Journal of Applied Meteorology*, **43** (12), 1834–1853.
- Houze Jr, R. A., 2014: *Cloud dynamics*. Academic press.
- Huang, P.-C., Y.-L. Chen, Y.-S. Liou, B.-C. Tsai, C.-C. Wu, and W. H. Hsu, 2023: STAMINA (Spatial-Temporal Aligned Meteorological INformation Attention) and FPL (Focal Precip Loss): Advancements in Precipitation Nowcasting for Heavy Rainfall Events. *Proceedings of the 32nd ACM International Conference on Information and Knowledge Management*, 854–863.
- Huffman, G. J., and Coauthors, 2020: Integrated multi-satellite retrievals for the global precipitation measurement (GPM) mission (IMERG). *Satellite precipitation measurement*, Springer, 343–353.
- Hunke, E., W. Lipscomb, P. Jones, A. Turner, N. Jeffery, and S. Elliott, 2017: CICE, The Los Alamos sea ice model. Tech. rep., Los Alamos National Lab.(LANL), Los Alamos, NM (United States).
- Hwang, Y., A. J. Clark, V. Lakshmanan, and S. E. Koch, 2015: Improved nowcasts by blending extrapolation and model forecasts. *Weather and Forecasting*, **30** (5), 1201–1217.
- Imhoff, R. O., C. C. Brauer, K.-J. van Heeringen, R. Uijlenhoet, and A. H. Weerts, 2022: Large-sample evaluation of radar rainfall nowcasting for flood early warning. *Water Resources Research*, **58** (3), e2021WR031591.
- Jin, Q., X. Zhang, X. Xiao, G. Meng, S. Xiang, C. Pan, and Coauthors, 2023: SpatioTemporal Inference Network for Precipitation Nowcasting With Multi-Modal Fusion. *IEEE Journal of Selected Topics in Applied Earth Observations and Remote Sensing*.

- Jolliffe, I. T., and D. B. Stephenson, 2012: *Forecast verification: a practitioner's guide in atmospheric science*. John Wiley & Sons.
- Joyce, R. J., and P. Xie, 2011: Kalman filter-based cmorph. *Journal of Hydrometeorology*, **12** (6), 1547–1563.
- Kendon, E., A. Prein, C. Senior, and A. Stirling, 2021: Challenges and outlook for convection-permitting climate modelling. *Philosophical Transactions of the Royal Society A*, **379** (2195), 20190547.
- Kendon, E. J., N. M. Roberts, C. A. Senior, and M. J. Roberts, 2012: Realism of rainfall in a very high-resolution regional climate model. *Journal of Climate*, **25** (17), 5791–5806.
- Kim, S., A. Sharma, C. Wasko, and R. Nathan, 2022: Linking total precipitable water to precipitation extremes globally. *Earth's Future*, **10** (2), e2021EF002473.
- Kingma, D. P., and J. Ba, 2014: Adam: A method for stochastic optimization. *arXiv preprint arXiv:1412.6980*.
- Kotsuki, S., K. Kurosawa, S. Otsuka, K. Terasaki, and T. Miyoshi, 2019: Global precipitation forecasts by merging extrapolation-based nowcast and numerical weather prediction with locally optimized weights. *Weather and Forecasting*, **34** (3), 701–714.
- Krizhevsky, A., I. Sutskever, and G. E. Hinton, 2012: Imagenet classification with deep convolutional neural networks. *Advances in neural information processing systems*, **25**.
- Kubota, T., and Coauthors, 2007: Global precipitation map using satellite-borne microwave radiometers by the GSMaP project: Production and validation. *IEEE Transactions on Geoscience and Remote Sensing*, **45** (7), 2259–2275.
- Kumar, A., T. Islam, Y. Sekimoto, C. Mattmann, and B. Wilson, 2020: Convcast: An embedded convolutional LSTM based architecture for precipitation nowcasting using satellite data. *Plos one*, **15** (3), e0230114.
- Kummerow, C. D., D. L. Randel, M. Kulie, N.-Y. Wang, R. Ferraro, S. Joseph Munchak, and V. Petkovic, 2015: The evolution of the Goddard profiling algorithm to a fully parametric scheme. *Journal of atmospheric and oceanic technology*, **32** (12), 2265–2280.

- LeCun, Y., Y. Bengio, and G. Hinton, 2015: Deep learning. *nature*, **521 (7553)**, 436–444.
- Lin, C., S. Vasić, A. Kilambi, B. Turner, and I. Zawadzki, 2005: Precipitation forecast skill of numerical weather prediction models and radar nowcasts. *Geophysical research letters*, **32 (14)**.
- Lin, L.-F., A. M. Ebtehaj, R. L. Bras, A. N. Flores, and J. Wang, 2015: Dynamical precipitation downscaling for hydrologic applications using WRF 4D-Var data assimilation: Implications for GPM era. *Journal of Hydrometeorology*, **16 (2)**, 811–829.
- Lin, L.-F., and Z. Pu, 2020: Improving near-surface short-range weather forecasts using strongly coupled land–atmosphere data assimilation with GSI-EnKF. *Monthly Weather Review*, **148 (7)**, 2863–2888.
- Lin, T.-Y., P. Goyal, R. Girshick, K. He, and P. Dollár, 2017: Focal loss for dense object detection. *Proceedings of the IEEE international conference on computer vision*, 2980–2988.
- Liu, C., K. Ikeda, G. Thompson, R. Rasmussen, and J. Dudhia, 2011: High-resolution simulations of wintertime precipitation in the Colorado Headwaters region: Sensitivity to physics parameterizations. *Monthly Weather Review*, **139 (11)**, 3533–3553.
- Liu, P., C. Li, Y. Wang, and Y. Fu, 2013: Climatic characteristics of convective and stratiform precipitation over the Tropical and Subtropical areas as derived from TRMM PR. *Science China Earth Sciences*, **56**, 375–385.
- Lorenc, A. C., N. E. Bowler, A. M. Clayton, S. R. Pring, and D. Fairbairn, 2015: Comparison of hybrid-4D-EnVar and hybrid-4D-Var data assimilation methods for global NWP. *Monthly Weather Review*, **143 (1)**, 212–229.
- MacKay, D. J., and D. J. Mac Kay, 2003: *Information theory, inference and learning algorithms*. Cambridge university press.
- McCormac, J., A. Handa, A. Davison, and S. Leutenegger, 2017: Semanticfusion: Dense 3d semantic mapping with convolutional neural networks. *2017 IEEE International Conference on Robotics and automation (ICRA)*, IEEE, 4628–4635.

- Mittermaier, M., and N. Roberts, 2010: Intercomparison of spatial forecast verification methods: Identifying skillful spatial scales using the fractions skill score. *Weather and Forecasting*, **25** (1), 343–354.
- Mnih, V., and Coauthors, 2015: Human-level control through deep reinforcement learning. *nature*, **518** (7540), 529–533.
- NCEP, 2021: The Global Forecast System (GFS) – Global Spectral Model (GSM). URL [https://www.emc.ncep.noaa.gov/emc/pages/numerical\\_forecast\\_systems/gfs/documentation\\_spectralgfs.php](https://www.emc.ncep.noaa.gov/emc/pages/numerical_forecast_systems/gfs/documentation_spectralgfs.php).
- Ning, L., F. P. Carli, A. M. Ebtehaj, E. Foufoula-Georgiou, and T. T. Georgiou, 2014: Coping with model error in variational data assimilation using optimal mass transport. *Water Resources Research*, **50** (7), 5817–5830.
- Niu, G.-Y., and Coauthors, 2011: The community Noah land surface model with multiparameterization options (Noah-MP): 1. Model description and evaluation with local-scale measurements. *Journal of Geophysical Research: Atmospheres*, **116** (D12).
- Otsuka, S., S. Kotsuki, and T. Miyoshi, 2016: Nowcasting with data assimilation: A case of global satellite mapping of precipitation. *Weather and Forecasting*, **31** (5), 1409–1416.
- Otsuka, S., S. Kotsuki, M. Ohhigashi, and T. Miyoshi, 2019: GSMaP RIKEN Nowcast: Global precipitation nowcasting with data assimilation. *Journal of the Meteorological Society of Japan. Ser. II*.
- Pan, X., Y. Lu, K. Zhao, H. Huang, M. Wang, and H. Chen, 2021: Improving Nowcasting of Convective Development by Incorporating Polarimetric Radar Variables Into a Deep-Learning Model. *Geophysical Research Letters*, **48** (21), e2021GL095302.
- Peng, H., F. Long, and C. Ding, 2005: Feature selection based on mutual information criteria of max-dependency, max-relevance, and min-redundancy. *IEEE Transactions on pattern analysis and machine intelligence*, **27** (8), 1226–1238.
- Pfreundschuh, S., I. Ingemarsson, P. Eriksson, D. A. Vila, and A. J. Calheiros, 2022: An improved near-real-time precipitation retrieval for Brazil. *Atmospheric Measurement Techniques*, **15** (23), 6907–6933.

- Powers, J. G., and Coauthors, 2017: The weather research and forecasting model: Overview, system efforts, and future directions. *Bulletin of the American Meteorological Society*, **98** (8), 1717–1737.
- Prein, A. F., and Coauthors, 2015: A review on regional convection-permitting climate modeling: Demonstrations, prospects, and challenges. *Reviews of geophysics*, **53** (2), 323–361.
- Pulkkinen, S., D. Nerini, A. A. Pérez Hortal, C. Velasco-Forero, A. Seed, U. Germann, and L. Foresti, 2019: Pysteps: an open-source Python library for probabilistic precipitation nowcasting (v1. 0). *Geoscientific Model Development*, **12** (10), 4185–4219.
- Putman, W. M., and S.-J. Lin, 2007: Finite-volume transport on various cubed-sphere grids. *Journal of Computational Physics*, **227** (1), 55–78.
- Ravirathinam, P., R. Ghosh, K. Wang, K. Xuan, A. Khandelwal, H. Dugan, P. Hanson, and V. Kumar, 2023: Spatiotemporal Classification with limited labels using Constrained Clustering for large datasets. *Proceedings of the 2023 SIAM International Conference on Data Mining (SDM)*, SIAM, 487–495.
- Ravuri, S., and Coauthors, 2021: Skilful precipitation nowcasting using deep generative models of radar. *Nature*, **597** (7878), 672–677.
- Rawat, W., and Z. Wang, 2017: Deep convolutional neural networks for image classification: A comprehensive review. *Neural computation*, **29** (9), 2352–2449.
- Reyniers, M., 2008: *Quantitative precipitation forecasts based on radar observations: Principles, algorithms and operational systems*. Institut Royal Météorologique de Belgique Brussel, Belgium.
- Robin, Y., P. Yiou, and P. Naveau, 2017: Detecting changes in forced climate attractors with Wasserstein distance. *Nonlinear Processes in Geophysics*, **24** (3), 393–405.
- Ronneberger, O., P. Fischer, and T. Brox, 2015: U-net: Convolutional networks for biomedical image segmentation. *Medical Image Computing and Computer-Assisted Intervention – MICCAI 2015*, N. Navab, J. Hornegger, W. M. Wells, and A. F. Frangi, Eds., Springer International Publishing, Cham, 234–241.

- Rosenfeld, D., and I. M. Lensky, 1998: Satellite-based insights into precipitation formation processes in continental and maritime convective clouds. *Bulletin of the American Meteorological Society*, **79** (11), 2457–2476.
- Schaefer, J. T., 1990: The critical success index as an indicator of warning skill. *Weather and forecasting*, **5** (4), 570–575.
- Shi, X., Z. Chen, H. Wang, D.-Y. Yeung, W.-K. Wong, and W.-c. Woo, 2015: Convolutional LSTM network: A machine learning approach for precipitation nowcasting. *Advances in neural information processing systems*, **28**.
- Shi, X., Z. Gao, L. Lausen, H. Wang, D.-Y. Yeung, W.-k. Wong, and W.-c. Woo, 2017: Deep learning for precipitation nowcasting: A benchmark and a new model. *Advances in neural information processing systems*, **30**.
- Skok, G., and N. Roberts, 2016: Analysis of fractions skill score properties for random precipitation fields and ECMWF forecasts. *Quarterly Journal of the Royal Meteorological Society*, **142** (700), 2599–2610.
- Sønderby, C. K., and Coauthors, 2020: Metnet: A neural weather model for precipitation forecasting. *arXiv preprint arXiv:2003.12140*.
- Sun, J., 2005: Convective-scale assimilation of radar data: progress and challenges. *Quarterly Journal of the Royal Meteorological Society: A journal of the atmospheric sciences, applied meteorology and physical oceanography*, **131** (613), 3439–3463.
- Sun, J., and Coauthors, 2014a: Use of NWP for nowcasting convective precipitation: Recent progress and challenges. *Bulletin of the American Meteorological Society*, **95** (3), 409–426.
- Sun, W., F. Su, and L. Wang, 2014b: Improving deep neural networks with multilayer maxout networks. *2014 IEEE Visual Communications and Image Processing Conference*, IEEE, 334–337.
- Tamang, S. K., A. Ebtehaj, P. J. Van Leeuwen, D. Zou, and G. Lerman, 2021: Ensemble Riemannian data assimilation over the Wasserstein space. *Nonlinear Processes in Geophysics Discussions*, **2021**, 1–26.

- Tamang, S. K., A. Ebtehaj, D. Zou, and G. Lerman, 2020: Regularized variational data assimilation for bias treatment using the Wasserstein metric. *Quarterly Journal of the Royal Meteorological Society*, **146 (730)**, 2332–2346.
- Toth, Z., and E. Kalnay, 1997: Ensemble forecasting at NCEP and the breeding method. *Monthly Weather Review*, **125 (12)**, 3297–3319.
- Trebing, K., T. Stanczyk, and S. Mehrkanoon, 2021: SmaAt-UNet: Precipitation nowcasting using a small attention-UNet architecture. *Pattern Recognition Letters*, **145**, 178–186, <https://doi.org/https://doi.org/10.1016/j.patrec.2021.01.036>, URL <https://www.sciencedirect.com/science/article/pii/S0167865521000556>.
- Villani, C., and Coauthors, 2009: *Optimal transport: old and new*, Vol. 338. Springer.
- Vissio, G., V. Lembo, V. Lucarini, and M. Ghil, 2020: Evaluating the performance of climate models based on Wasserstein distance. *Geophysical Research Letters*, **47 (21)**, e2020GL089385.
- Wallace, J. M., and P. V. Hobbs, 2006: *Atmospheric science: an introductory survey*, Vol. 92. Elsevier.
- Wang, Y., M. Long, J. Wang, Z. Gao, and P. S. Yu, 2017: Predrnn: Recurrent neural networks for predictive learning using spatiotemporal lstms. *Advances in neural information processing systems*, **30**.
- Wang, Y., H. Wu, J. Zhang, Z. Gao, J. Wang, S. Y. Philip, and M. Long, 2022: Predrnn: A recurrent neural network for spatiotemporal predictive learning. *IEEE Transactions on Pattern Analysis and Machine Intelligence*, **45 (2)**, 2208–2225.
- Yang, L., Y. Fan, and N. Xu, 2019: Video instance segmentation. *Proceedings of the IEEE/CVF International Conference on Computer Vision*, 5188–5197.
- Zhang, S. Q., M. Zupanski, A. Y. Hou, X. Lin, and S. H. Cheung, 2013: Assimilation of precipitation-affected radiances in a cloud-resolving WRF ensemble data assimilation system. *Monthly Weather Review*, **141 (2)**, 754–772.

- Zhang, X., Y. Yang, B. Chen, and W. Huang, 2021: Operational precipitation forecast over China using the weather research and forecasting (WRF) model at a gray-zone resolution: impact of convection parameterization. *Weather and Forecasting*, **36 (3)**, 915–928.
- Zhang, Y., M. Long, K. Chen, L. Xing, R. Jin, M. I. Jordan, and J. Wang, 2023: Skilful nowcasting of extreme precipitation with NowcastNet. *Nature*, **619 (7970)**, 526–532.
- Zhang, Y., and K. Wang, 2021: Global precipitation system size. *Environmental Research Letters*, **16 (5)**, 054 005.